



**HAL**  
open science

# Early accretion of planetesimals unraveled by the thermal evolution of the parent bodies of magmatic iron meteorites

Edouard Kaminski, Angela Limare, Balthasar Kenda, Marc Chaussidon

► **To cite this version:**

Edouard Kaminski, Angela Limare, Balthasar Kenda, Marc Chaussidon. Early accretion of planetesimals unraveled by the thermal evolution of the parent bodies of magmatic iron meteorites. *Earth and Planetary Science Letters*, 2020, 548, pp.116469. 10.1016/j.epsl.2020.116469 . insu-02931908

**HAL Id: insu-02931908**

**<https://insu.hal.science/insu-02931908>**

Submitted on 12 Aug 2021

**HAL** is a multi-disciplinary open access archive for the deposit and dissemination of scientific research documents, whether they are published or not. The documents may come from teaching and research institutions in France or abroad, or from public or private research centers.

L'archive ouverte pluridisciplinaire **HAL**, est destinée au dépôt et à la diffusion de documents scientifiques de niveau recherche, publiés ou non, émanant des établissements d'enseignement et de recherche français ou étrangers, des laboratoires publics ou privés.



Distributed under a Creative Commons Attribution 4.0 International License

# Early accretion of planetesimals unraveled by the thermal evolution of the parent bodies of magmatic iron meteorites

Edouard Kaminski<sup>a,\*</sup>, Angela Limare<sup>a</sup>, Balthasar Kenda<sup>a</sup>, Marc Chaussidon<sup>a</sup>

<sup>a</sup>*Université de Paris, Institut de Physique du Globe de Paris, CNRS, 1 rue Jussieu, F-75005 Paris, France*

---

## Abstract

The timing of formation of 100-300 km size planetesimals in the protoplanetary disk remains largely unconstrained. Recent models show that gravitational collapse of boulders in overdense regions of a dusty accretion disk can overcome the meter-sized barrier and lead to rapid formation of planetesimals with size of several km that further grow by pebble accretion. Hf/W ages indicate that the first large planetesimals to form could be the parent bodies of magmatic iron meteorites. These ages have been so far used to constrain timing of accretion considering (i) instantaneous accretion, and (ii) purely conductive heat transfer in the planetesimal. To relax these hypotheses we model the thermal evolution of a planetesimal in course of accretion and we take into account the possibility of convection onset. Our model is further based on considering the possibility of a common thermal evolution for all the parent bodies of iron meteorites. Within that framework we show that

---

\*Corresponding author

*Email address:* [kaminski@ipgp.fr](mailto:kaminski@ipgp.fr) (Edouard Kaminski)

the planetesimals could have grown following a universal accretion law starting at the very beginning of the history of the disk by a nearly instantaneous formation of  $60\pm 30$  km size nuclei, followed by a growth via pebble accretion at a much slower pace to reach final sizes of 150–300 km in about 3 Myr. In this universal scenario, complete melting and total differentiation are not bound to happen in the parent body due to the continuous accretion of cold pebbles. The model, though calibrated here on iron meteorites, is general and can in principle be applied to other types of planetesimals such as for instance the parent bodies of CV chondrites.

*Keywords:* planetesimals, accretion, convection, analog experiments, magmatic iron meteorites

---

## 1. Introduction

The formation of planetesimals is a crucial stage in the evolution of the protoplanetary disk that leads from dust to planets. Some of its fundamental aspects remain the object of debate, such as the range in initial and final sizes of the planetesimals, and more generally their mechanism and rate of accretion (e.g., Xie et al., 2010; Morbidelli and Raymond, 2016; Birnstiel et al., 2016).

A key and long-standing question has been the process of formation of the initial seeds of the planetesimals. Models of collision between aggregates of dust held by electrostatic forces fail to produce planetesimals, because the particles start to bounce upon collision when they reach few centimeters and migrate rapidly toward the star as they grow (e.g., Morbidelli and Raymond, 2016). Meter-size boulders migrate so fast that they are eventually

14 lost to the sun. One way to overcome this meter-size barrier (Weidenschilling,  
15 1977) is to consider a weakly turbulent nebula where large and dense clumps  
16 of chondrules can form on the smallest scale of the flow, and be preserved  
17 by self-gravity to later produce planetesimals by sedimentation towards their  
18 center (Cuzzi et al., 2008). Numerical simulations (e.g., Johansen et al., 2015;  
19 Simon et al., 2017) show that other mechanisms such as quasi-stable pres-  
20 sure bumps and/or streaming instabilities can produce gravitationally-bound  
21 pebble-swarms collapse under their own gravity, yielding initial planetesimal  
22 sizes up to many tens of kilometers across.

23       Once the seeds of planetesimals are formed, they are supposed to con-  
24 tinue to grow by pebble accretion (Johansen and Lambrechts, 2017). This  
25 mechanism is controlled by the interplay between gravity, aerodynamics de-  
26 flection and gas drag (e.g., Ormel and Klahr, 2010). Models predictions give  
27 the minimum planetesimal radius for the onset of pebble accretion as well  
28 as the growth timescales for a given radius at a given distance from the sun  
29 (Visser and Ormel, 2016). But theses models have not been used yet to  
30 predict complete accretion scenarii for the planetesimals and to confront the  
31 output with independent constraints.

32       Constraints on the accretion of planetesimals in the disk can be obtained  
33 by astronomical observations (e.g., van der Marel and et al., 2013; Delbo'  
34 et al., 2017) as well as by the study of meteoritic fragments that sampled the  
35 early stages of the disk evolution during which planetesimals formed. The  
36 very early ages demonstrated by Hf/W studies of iron meteorites presumably  
37 originating from planetesimals accreted inside and outside the orbit of the  
38 growing Jupiter, indicate that these planetesimals and a Jupiter's core of  $\approx 20$

39 Earth mass may have formed within the first million year (Myr) of the solar  
40 system (Birnstiel et al., 2016; Kruijer et al., 2014, 2017). At variance, the  
41 presence in chondritic meteorites of Ca-, Al-rich inclusions (CAIs) and chon-  
42 drules spanning in age the first 4 Myr of the solar system (e.g., Villeneuve  
43 et al., 2009) shows that their parent planetesimals completed their accre-  
44 tion significantly later. Because no phenomenological law for planetesimal  
45 accretion has ever been derived from data on meteorites, the first principles  
46 behind these different accretion times still remain inaccessible.

47 One way to unravel the accretion history of planetesimals is to study their  
48 thermal evolution, which is strongly controlled by their size (e.g., Merk et al.,  
49 2002) that sets the ratio between internal production of energy (proportional  
50 to the cube of the size) and the surface heat loss (proportional to the square of  
51 the size). Previous models have essentially considered that the surface heat  
52 loss could be estimated based on a conductive profile in the planetesimal  
53 (e.g., Ghosh et al., 2003). It has been shown however that melting-induced  
54 convection could occur  $\approx 1$  Myr after the accretion of a planetesimal (Hevey  
55 and Sanders, 2006). The conductive hypothesis is thus not valid over the  
56 whole thermal history of a planetesimal and more efficient heat transfer by  
57 convection must be taken into account. To our knowledge, the recent study  
58 of Lichtenberg et al. (2016) is the only one to explicitly model convection  
59 in the planetesimal, using 2D and 3D numerical simulations. However this  
60 study considers instantaneous accretion and does not tackle the question  
61 of the thermal evolution of the planetesimal in the route of accretion. We  
62 propose to do so in the present study by using scaling laws for the transient  
63 thermal evolution of an internally heated convective body validated by lab-

64 scale experiments.

## 65 **2. Thermal evolution of a planetesimal in the course of accretion:** 66 **principles and constraints**

### 67 *2.1. Conservation of energy*

68 The average internal temperature  $T(t)$  of a spherical body of radius  $R(t)$   
69 can be defined based on its total thermal energy  $E(t)$  as

$$T(t) = \frac{E(t)}{4/3\pi\rho C_p R^3(t)}, \quad (1)$$

70 with  $\rho$  the density and  $C_p$  the specific heat (Table 1). The time evolution of  
71 this average internal temperature is given by the balance between internal  
72 radioactive heating due to decay of short-lived  $^{26}\text{Al}$ ,  $H(t)$ , and the surface  
73 heat loss,  $Q_s(t)$ ,

$$\rho C_p \frac{4}{3}\pi \frac{dR^3(t)T(t)}{dt} = \frac{4}{3}\pi R^3(t)H(t) - 4\pi R^2(t)Q_s(t) + E_{int}, \quad (2)$$

74 where  $E_{int}=E_{lat}+E_a$  is a term corresponding to the heat absorbed by partial  
75 melting ( $E_{lat}$ ) or brought by surface impacts ( $E_a$ ), as discussed later (Section  
76 3.1). For a given accretion law  $R(t)$ ,  $T(t)$  can be calculated using the energy  
77 balance equation (2) if the surface heat flux  $Q_s(t)$  is known. Equivalently,  
78 but the other way around, if a thermal record  $T(t)$  is given, equation 2 can  
79 be inverted to obtain the accretion curve  $R(t)$ .

80 In the purely conductive regime  $Q_s(t)$  is analytically known (Carslaw  
81 and Jaeger, 1959, p. 245). In a convective regime, the determination of  
82  $Q_s(t)$  requires either the numerical resolution of the full set of conservative  
83 equations in the convective fluid (Lichtenberg et al., 2016), or the use of a

84 scaling law relating the surface heat flux to the fluid properties, the internal  
85 heating rate, and the geometry of the system; an approach we will detail and  
86 follow in section 3.

## 87 *2.2. Constraints brought by the magmatic iron meteorites*

### 88 *2.2.1. Temperature and age of formation*

89 The  $^{182}\text{Hf}$ - $^{182}\text{W}$  age of magmatic iron meteorites can be taken as the for-  
90 mation time of their core, or, more generally, the time of metal-silicate differ-  
91 entiation and metal segregation (Lee and Halliday, 1997; Kleine et al., 2002;  
92 Qin et al., 2008; Kruijer et al., 2014). Data for five groups of magmatic iron  
93 meteorites (IIAB, IID, IIIAB, IVA, IVB) provide ages spanning from  $0.7\pm 0.3$   
94 Myr after CAIs for IIAB to  $3.1\pm 0.8$  Myr after CAIs for IIB (Kruijer et al.,  
95 2014). Their temperatures of formation, taken as the liquidus temperature  
96 of the iron-sulfur alloy, range from 1325 °C to 1615 °C as a function of their  
97 sulfur content (see Table 2 from Supplementary material). We note in Fig-  
98 ure 1 that a single exponential function fits within errors bars the data on the  
99 five groups of magmatic iron meteorites  $T(t) = T_{\infty}[1 - \exp(-t/\tau)]$ . We used  
100 an Orthogonal Distance Regression (ODR) method based on a Levenberg-  
101 Marquardt type algorithm that allows non-linear fitting with errors on both  
102 variables, and we obtained the following values:  $\tau = 0.424 \pm 0.108$  Myr and  
103  $T_{\infty} = 1524 \pm 46$  °C. Rather than considering a specific thermal evolution  
104 hence a somewhat open ended accretion history for each magmatic iron me-  
105 teorite, such a unique fit opens the possibility to look for a tightly constrained  
106 universal accretion scenario that can explain all the data. To that aim, we  
107 will use in the following (section 4) the best fitting exponential evolution of  
108 the temperature to obtain accretion curves  $R(t)$  - if they exist - consistent

109 with this thermal evolution.

### 110 *2.2.2. Metallographic cooling rates*

111 To further constrain the accretion curves, we will rely on the metallo-  
112 graphic cooling rates to infer the size of the parent bodies of magmatic iron  
113 meteorites. These correspond to the latest (conductive) cooling phase of a  
114 metallic pocket (or core) once it has solidified. They are thus independent  
115 from the thermal models considered in this study which will only describe  
116 the heating (and convective) stage of the accreting planetesimals. The size  
117 of the planetesimals are poorly constrained and have been estimated based  
118 on two assumptions (see Table 3 from Supplementary material).

119 The IVA meteorites have the highest cooling rates, interpreted as result-  
120 ing from the conductive cooling of a  $150\pm 50$  km metallic core with its mantle  
121 ripped off, yielding a parent body size of  $\approx 300$  km (Yang et al., 2008). Cool-  
122 ing rates for IVB meteorites give a parent body size of  $140\pm 30$  km (Yang  
123 et al., 2010).

124 Other magmatic iron meteorites display smaller cooling rates (Yang and  
125 Goldstein, 2006; Goldstein et al., 2009) which reflects the insulating effect  
126 of a mantle and possibly of a regolith. Their size depends on the thickness  
127 and thermal properties of the rocky envelopes around the core (Haack et al.,  
128 1990). Based on the recorded cooling rates and on Figure 7.1 of McSween  
129 (1999) we estimate the radii as  $125\pm 50$  km for IIIAB,  $235\pm 65$  km for IID,  
130 and  $165\pm 65$  km for IIAB.

131 **3. Transient thermal evolution in an internally heated convective**  
 132 **system**

133 The resolution of the energy balance equation 2 requires a knowledge of  
 134 the surface heat flux  $Q_s$  which is different in a conductive and in a convective  
 135 thermal regime. In the case of Rayleigh-Bénard convection, where convec-  
 136 tion results from cooling at the top of the system and heating at its base,  
 137 scaling laws are expressed using the Nusselt number,  $Nu$ , defined as the ra-  
 138 tio between the surface heat flux measured in the convective regime and the  
 139 surface heat flux in the conductive regime. At steady state,  $Nu$  scales as the  
 140  $1/3^{\text{rd}}$  power of the Rayleigh number of the well-mixed convective layer. In in-  
 141 ternally heated fluids, convection depends on the so called Rayleigh-Roberts  
 142 number, defined as

$$Ra_H = \frac{\rho g \alpha H R^5}{k \kappa \nu}, \quad (3)$$

143 with  $g$  the gravity,  $\alpha$  the coefficient of thermal expansion,  $k$  the thermal con-  
 144 ductivity,  $\kappa$  the thermal diffusivity and  $\nu$  the kinematic viscosity (Table 1).  
 145 In this setting, at steady state the Nusselt number is unity and the average  
 146 internal temperature at steady state in an internally heated convective fluid  
 147 (Parmentier and Sotin, 2000) follows a power scaling law

$$T/T_H = c Ra_H^{-\beta}, \quad (4)$$

148 with  $c$  and  $\beta$  dimensionless constants, and  $T_H = \rho H R^2 / k$  the internal heat-  
 149 ing temperature scale with  $R$  now the fluid thickness in the experiments.  
 150 Experiments yield  $\beta=1/4$  at steady state (Limare et al., 2015), in agreement  
 151 with theory (Vilella and Kaminski, 2017). In principle, this law holds for  
 152 the temperature difference across the unstable boundary layer. It turns out,

153 however, that the temperature at the edge of the boundary layer and the  
 154 average internal temperature can both be scaled to  $Ra_H^{-1/4}$  and hence are  
 155 proportional to one another (Vilella et al., 2018; Limare et al., 2015). We  
 156 confirmed that this scaling is valid in our experiments over several orders  
 157 of magnitude in  $Ra_H$  as can be seen in the accompanying MethodsX paper  
 158 (Limare et al., 2020) with  $c=3.45\pm 0.15$ .

159 As we consider the transient regime in the experiments, i.e., before the  
 160 steady state is reached, a secular term  $dT/dt$  has to be introduced in the  
 161 scaling law. Assuming that the secular term can be treated as an additional  
 162 contribution to internal heating, equation 4 becomes

$$T = cRa_H^*{}^{-\beta} \rho \left( H - C_p \frac{dT}{dt} \right) R^2/k, \quad (5)$$

163 where  $Ra_H^*$  is a modified Rayleigh-Roberts number defined as

$$Ra_H^* = \frac{\rho g \alpha \left( H - C_p \frac{dT}{dt} \right) R^5}{k \kappa \nu}. \quad (6)$$

164 The two previous equations can be combined to yield an expression for the  
 165 time derivative of the average internal temperature,

$$\rho C_p \frac{dT}{dt} = \rho H - \left( \frac{kT}{cR^2} \right)^{\frac{1}{1-\beta}} \left( \frac{g\alpha R^5}{k\kappa\nu} \right)^{\frac{\beta}{1-\beta}}. \quad (7)$$

166 Further noting that the conservation of energy per unit surface writes

$$\rho C_p R \frac{dT}{dt} = \rho H R - Q_s, \quad (8)$$

167 we obtain an expression for the surface heat flux in the convective regime,

$$Q_s = \left( \frac{kT}{cR} \right)^{\frac{1}{1-\beta}} \left( \frac{g\alpha R^4}{k\kappa\nu} \right)^{\frac{\beta}{1-\beta}}, \quad (9)$$

168 that is found in very good agreement with the experimental results over  
 169 several orders of magnitude (Limare et al., 2020). We will now apply these  
 170 experimentally validated theoretical results to systems where the secular evo-  
 171 lution of the average internal temperature is also related to the time evolution  
 172 of internal heating rate as in the case of a planetesimal.

### 173 *3.1. Adaptation of the scaling-laws to the thermal evolution of a planetesimal*

174 To apply the experimentally determined scaling law to the modeling of the  
 175 thermal evolution of a planetesimal, we need to consider several differences  
 176 between the experimental setting and the natural case. First, we multiply  
 177 the literal expression we have obtained in equation (9) by a factor 1/3 corre-  
 178 sponding to a spherical geometry, as established by Deschamps et al. (2012).  
 179 Second, we take into account the decreasing heating rate induced by the pro-  
 180 gressive disintegration of  $^{26}\text{Al}$  and the implications on the material properties  
 181 of a planetesimal given in Table 1.

182 In the parent body, viscosity is not constant but changes as a function of  
 183 the average internal temperature and – when relevant – the fraction of melt,  
 184 and is given by

$$\mu = \mu_0 f(\phi^{melt}) \exp\left(\frac{E_{act}}{R_g T} - \frac{E_{act}}{R_g T_0}\right), \quad (10)$$

185 where  $\mu_0$  is a reference viscosity at  $T_0=1000$  °C (that will be set between  
 186  $10^{18}$  and  $10^{21}$  Pa s, see section 4),  $R_g$  is the ideal gas constant,  $E_{act}$  is the  
 187 activation energy (Table 1), and  $f(\phi^{melt})$  is defined as

$$f(\phi^{melt}) = \exp(-\sigma_{sil}\phi_{sil}^{melt}) \exp(-\sigma_{Fe}\phi_{Fe}^{melt}), \quad (11)$$

188 where the fractions of melt are taken as a linear function of temperature,

$$\phi_{sil,Fe}^{melt} = \frac{T - T_s^{sil,Fe}}{T_l^{sil,Fe} - T_s^{sil,Fe}}, \quad (12)$$

189 if  $T_s^{sil,Fe} < T < T_l^{sil,Fe}$  with  $T_s^{sil,Fe}$  and  $T_l^{sil,Fe}$  the solidus and liquidus  
 190 temperature of silicate and metal, respectively, and  $\sigma_{Fe}=4$  and  $\sigma_{sil}=21$  (Scott  
 191 and Kohlstedt, 2006; Hustoft et al., 2007).

192 Because in silicate bodies the viscosity is strongly temperature dependent,  
 193 we must also account for the presence of a conductive viscous lid at the top  
 194 of the convective system (e.g. Davaille and Jaupart, 1993). In that case, four  
 195 additional parameters have to be introduced: the thickness of the lid and  
 196 the temperature drop across the lid, the thickness of the thermal boundary  
 197 layer at the top of the convective fluid and the temperature drop across the  
 198 thermal boundary layer. The thickness and temperature drop across the  
 199 thermal boundary layer at the top of the convective fluid are given by well  
 200 established scaling laws for thermal convection with large viscosity variations  
 201 (Davaille and Jaupart, 1993; Choblet and Sotin, 2000). These laws introduce  
 202 a “viscous scale”  $\Delta T_{visc}$  for the temperature,

$$\Delta T_{visc}(T) = -2.21 \frac{\mu(T)}{d\mu/dT(T)}. \quad (13)$$

203 The thickness  $\delta_{lid}$  of the viscous lid and the temperature  $T_{lid}$  at its base are  
 204 then obtained by imposing the continuity of temperature and heat flux at the  
 205 base of the lid. To that aim we use  $T = T_{lid} + \Delta T_{visc}$  as the average internal  
 206 temperature of the convective fluid and  $\delta_{lid} = kT_{lid}/Q_s$ , while replacing  $R$  by  
 207  $R - \delta_{lid}$  in equation (9).

208 The energy absorbed by partial melting,  $E_{lat}$ , and the energy brought by  
 209 surface impacts during accretion,  $E_a$ , are the last ingredients to take into

210 account in the conservation of energy in the case of a planetesimal. The rate  
 211 of heat absorption by partial melting is given by

$$E_{lat} = L_{Sil} \frac{d\xi_{Sil}}{dt} + L_{Fe} \frac{d\xi_{Fe}}{dt}, \quad (14)$$

212 with  $L_{Sil}$  and  $L_{Fe}$  the latent heat of the silicate and metal (Table 1), respec-  
 213 tively, and  $\xi_{Sil}$  and  $\xi_{Fe}$  their melt fraction. The rate of variation of the melt  
 214 fractions for  $T_s^{sil,Fe} < T < T_l^{sil,Fe}$  is derived from equation (12) and writes

$$\frac{d\xi^{sil,Fe}}{dt} = \frac{dT/dt}{T_l^{sil,Fe} - T_s^{sil,Fe}}, \quad (15)$$

215 with  $T_s^{sil}=1150$  °C and  $T_s^{Fe}=990$  °C the silicate solidus and the Fe-FeS eutec-  
 216 tic, respectively, and  $T_l^{sil}=1800$  °C and  $T_l^{Fe}=1615$  °C for the silicate liquidus  
 217 and the pure Fe melting temperature, respectively. To take into account  
 218 surface impacts, we further consider that an impactor of mass  $M_i$  and tem-  
 219 perature  $T_i$  brings a gravitational energy  $E_G = GMM_i/R$ , with  $M$  and  
 220  $R$  the mass and radius of the target, respectively, and a thermal energy  
 221  $E_T = M_i C_P T_i$ . The fraction of energy that is transferred to the target rather  
 222 than radiated into space,  $E_a$ , is then set to a nominal fraction of 30% of  
 223  $(E_G + E_T)$  similar to the value used by Sramek et al. (2012). The effect of  
 224 this fraction is discussed in the Supplementary Material Figure 11.

## 225 **4. Accretion curve of the parent bodies of the magmatic iron me-** 226 **teorites from their thermal evolution**

### 227 *4.1. Instantaneous accretion*

228 As a first step in the study of the thermal evolution of planetesimals we  
 229 consider, as in previous models, instantaneous accretion and a purely conduc-  
 230 tive model. To be consistent with the sizes inferred from the metallographic

231 cooling rates we calculate the thermal evolution of a 300 km body as a func-  
232 tion of its time of accretion. We further consider a constant temperature of  
233 0 °C at the surface of the planetesimal. The results shown in the inset of  
234 Figure 2 imply that the parent bodies of non-carbonaceous magmatic iron  
235 meteorites accreted earlier ( $\approx 0.5$  Myr after CAIs formation) than the ones  
236 of carbonaceous magmatic iron meteorites ( $\approx 1$  Myr after CAIs formation).  
237 These results are consistent with the conclusions obtained for a 40 km body  
238 by Kruijer et al. (2014) which shows that within the framework of instanta-  
239 neous accretion and a purely conductive model the size of the body is not a  
240 key parameter for the thermal evolution.

241 Conductive models predict extreme temperatures in the planetesimals,  
242 larger than the liquidus of the metal and silicate phases, hence total melt-  
243 ing and differentiation of the non-carbonaceous magmatic iron meteorites  
244 (inset in Figure 2). Hence at least melting-induced convection should be  
245 taken into account in the thermal modeling. Both the increase of tempera-  
246 ture and the occurrence of melting actually decrease the viscosity (Supple-  
247 mentary Material Figure 8) and increase the value of the Rayleigh-Roberts  
248 number in the planetesimal. We obtain that the critical value for convection,  
249  $Ra_{H,cr} = 5758$  for a rigid boundary condition at the surface (Schubert et al.,  
250 2001), is reached at  $\approx 0.1$  Myr after CAIs (if accretion also starts at CAIs).  
251 Once  $Ra_H \geq Ra_{H,cr}$  convection should start. However, in a fluid with a  
252 strongly temperature dependent viscosity the onset of convection is signifi-  
253 cantly delayed (Davaille and Jaupart, 1993; Choblet and Sotin, 2000). We  
254 calculate the onset time of convection using the scaling given by experiments  
255 and numerical simulations (Davaille and Jaupart, 1993; Choblet and Sotin,

256 2000),

$$t_0 = \frac{1}{\pi} \frac{R^2}{\kappa} \left( \frac{Ra_{H,cr}}{Ra_H} \right)^{-2/3} \left( \frac{T}{\Delta T_{visc}} \right)^{8/3}. \quad (16)$$

257 The onset time evolves as a function of time following the increase of tem-  
258 perature in the planetesimal. We consider that convection starts when the  
259 age of the body becomes larger than  $t_0$  and we obtained an onset time of  
260  $\approx 0.2$  Myr. This can be taken as an upper bound as convection may start  
261 as soon as some melt segregation of iron triggers a density contrast driven  
262 Rayleigh-Taylor instability.

263 Thermal evolution in the case of instantaneous accretion, when convection  
264 is taken into account, is shown in Figure 2. Convection increases heat transfer  
265 in the body and results in significantly cooler average internal temperatures  
266 than in the purely conductive case. But the main conclusions reached in the  
267 conductive case still hold: the parent body of non-carbonaceous magmatic  
268 iron meteorites accreted earlier and underwent a hotter thermal evolution  
269 leading to total melting and complete differentiation. Convection does not  
270 rule out the capability of instantaneous accretion models to explain the mag-  
271 matic iron meteorites recorded ages and temperatures. Instantaneous accre-  
272 tion cannot however yield the common thermal evolution we have proposed  
273 Figure 1 and we will look now for accretion scenarios that can produce it.

#### 274 4.2. Continuous pebbles accretion

275 Using the time evolution of the average internal temperature proposed in  
276 Figure 1, we invert the energy balance equation 2 as a function of the thermal  
277 regime (conduction or convection) to obtain the accretion curves  $R(t)$ . In  
278 this case  $E_{int}=E_{lat}$  since  $E_a$  can be considered 0 for pebble accretion. Within

279 our framework, the free parameter in the inversion routine is the initial size  
280 of the planetesimal,  $R_0$ , that we will refer to as the nucleus, produced by  
281 gravitational collapse at the early beginning of the accretion. Because this  
282 phenomenon is very rapid compared to the time scale of the thermal evo-  
283 lution recorded by the magmatic iron meteorites, it can be considered as  
284 instantaneous in the present model.

285 In the first stage of accretion, the radius of the body is small and heat  
286 transfer occurs by conduction. For the sake of the argument we first con-  
287 sider a purely conductive regime to obtain  $R(t)$  from the required thermal  
288 evolution (figure 1). The results of the inversion are shown in figure 3 for a  
289 nucleus radius of 35 and 90 km. Based on these results we can calculate the  
290 evolution of  $Ra_H$  during the accretion of the body (Supplementary Material  
291 Figure 9) and further consider the influence of convection on the model pre-  
292 dictions. We calculate the onset time of convection along the accretion curve  
293 using the scaling of equation 16. We consider that convection starts (hence  
294 that Equation 9 applies) when the age of the body becomes larger than the  
295 onset time.

296 Figure 3 shows two examples of accretion curves resulting from the inver-  
297 sion of the time evolution of the average internal temperature once convec-  
298 tion has been introduced. The shape of the accretion curve is the same as in  
299 the case of a purely conductive regime (notably because the initial thermal  
300 regime is always conductive). However, because convection corresponds to  
301 a more efficient heat transfer, it is not possible in this regime to reach the  
302 thermal plateau observed at large times in Figure 1 if cold pebbles continue  
303 to accrete at the surface of the planetesimal.

304 In some cases it is even necessary that the radius of the body decreases  
305 in order to counterbalance convection-induced cooling. This is due to the  
306 fact that the internal energy varies with volume (which depends on the third  
307 power of radius) and the cooling rate is proportional to the surface (second  
308 power of radius). Due to convection the body might cool too fast, therefore  
309 the model calculates a radius that start to diminish in order to restore the  
310 almost constant temperature. This effect is more important for low values of  
311 initial radius (cooling/internal heat  $\sim 1/R$ ).

312 This decrease of radius can correspond either to some erosion, or to sin-  
313 tering at the end of accretion due to compaction of the planetesimal following  
314 partial melting. In the following we shall reject the accretion curves yielding  
315 to more than 10% of sintering as this is the bulk porosity value we consider in  
316 the present model. Based on all the constraints we conclude that the nucleus  
317 size of the parent body was between 35 and 90 km (figure 3).

318 As already mentioned, accretion curves depend only on the initial (nu-  
319 cleus) size  $R(t = 0) = R_0$ . When made dimensionless by dividing the radius  
320 of the body by its final value, all acceptable solutions (i.e., fitting both the  
321 thermal evolution recorded by the magmatic iron meteorites and their sizes)  
322 appear to share the same evolution (figure 4). This implies that both the  
323 shape of the accretion curve, and the associated thermal evolution, do not de-  
324 pend on the final size of the body (which itself depends on the initial nucleus  
325 radius), and the growth curves in figures 3 follow a single parameterized ac-  
326 cretion law (figure 4). Three stages of evolution can be introduced to describe  
327 the universal dimensionless accretion curve: (i) an initial quasi-instantaneous  
328 accretion of a nucleus with  $35 \leq R_0 \leq 90$  km, too fast to be resolved at the

329 scale of our model, (ii) a following slower accretion that reaches a plateau  
330 or even ends at  $\approx 3$  Myr, and (iii) a sintering due to the compaction of the  
331 planetesimal following partial melting. Compared to the more simple case  
332 of a purely conductive regime, the end of accretion at  $\approx 3$  Myr appears well  
333 resolved in the complete model including convection.

## 334 5. Discussion

### 335 5.1. *Alternative accretion scenarios*

336 To evaluate further the robustness of our model predictions, we study two  
337 alternative accretion scenarios: (i) successive collisions with impactors with  
338 sizes of tens of kilometers, and (ii) the fragmentation of a parent body.

339 In scenarios of discontinuous accretion, the planetesimal grow through  
340 successive collisions with impactors of a given size  $R_i$ . Here we consider that  
341 the impactors are formed with their final size  $R_i$  at  $t=0$  and we follow their  
342 average internal temperature using the conservation of energy as given by  
343 equation 2. We model two different types of accretion: orderly or runaway  
344 (figure 5). The resulting thermal evolution is illustrated figure 5 for a fi-  
345 nal parent body radius of 300 km and  $R_i=40$  km or  $R_i=10$  km. None of  
346 these scenarios yield a thermal evolution consistent with the magmatic iron  
347 meteorites record.

348 The results of scenario of discontinuous accretion – in the case of large  
349 impactors – are a function of the fraction of energy that is transferred to the  
350 parent body during accretion. We study the influence of this parameter for  
351 the thermal evolution corresponding to orderly accretion of impactors of 40  
352 km formed at time 0 producing a final body of 300 km in 4 My (Supple-

353 mentary Material Figure 11). We obtain that in the case of a perfect energy  
354 transfer to the parent body, or in the case of total loss of the impactor en-  
355 ergy to space, the thermal evolution predicted is not consistent with the  
356 constraints provided by the magmatic iron meteorites. We can then con-  
357 clude that our preferred scenario of continuous accretion is both robust and  
358 the only one able to yield a thermal evolution consistent with the constraints  
359 provided by the magmatic iron meteorites.

360 In the alternative scenario of fragmentation, the planetesimal has a large  
361 size at time 0 and is later fragmented into smaller bodies. For the sake of the  
362 argument we consider here an initial body size of 300 km, but the conclusions  
363 we reach are general. Because of the large initial size, the early thermal  
364 evolution is very fast, the surface heat loss ( $\propto R^2$ ) being much smaller than  
365 the internal heat sources ( $\propto R^3$ ). As a consequence total melting occurs early,  
366 even before the formation of IIAB (Supplementary Material Figure 12). The  
367 most favorable end member fragmentation scenario would be a very early  
368 fragmentation into small bodies, but this would imply in turn a subsequent  
369 episode of continuous accretion and would be equivalent to the formation of  
370 a nucleus followed by continuous pebbles accretion.

## 371 *5.2. Sensibility of the model of pebbles accretion with respect to model pa-* 372 *rameters*

373 Figure 3 shows that taking into account convection in a planetesimal  
374 under continuous accretion has a small impact on model prediction, limited  
375 to an end of accretion delayed from  $\approx 3$  Myr to  $\approx 4$  Myr. This reflects the  
376 strong control of the model outputs by the thermal evolution of Figure 1. As  
377 discussed above, this rather “cold” thermal evolution results mainly from the

378 accretion of cold pebbles, and the accretion curve is only tuned as a function  
379 of the thermal regime. This implies that the model predictions are robust  
380 and do not change significantly when we change the parameters used in the  
381 scaling laws. For example, a change of the reference viscosity by an order  
382 of magnitude has an almost negligible effect (Figure 3). We obtain also a  
383 negligible effect of a 50 % change in the values of activation energy and of  
384 melt sensitivities  $\sigma_{Fe}$  and  $\sigma_{sil}$ , or for a surface temperature of -150 °C instead  
385 of 0 °C (Supplementary Material Figure 10).

386 We also allowed the system to differentiate, considering iron segregation  
387 and migration towards the center of the parent body to form a metallic core.  
388 There are three effects of differentiation for the convecting silicate mantle:  
389 (i) a prefactor in the Rayleigh number (Equation 3) equal to  $(1 + f + f^2)/3$ ,  
390 where  $f = R_{core}/R$  (Deschamps et al., 2012) with  $R_{core}$  the core radius given  
391 by the mass fraction of metal, (ii) a concentration of the heat source, hence  
392 an increase of  $H(t)$ , in the mantle, as no Aluminium is partitioned into the  
393 core, and (iii) a decrease of its thickness from  $R$  to  $D = R - R_{core}$ . The two  
394 last effects tend to counterbalance each other and the resulting bulk impact  
395 of the differentiation on the accretion curves is not significant, as can be seen  
396 in Figure 6.

### 397 *5.3. Comparison with astrophysical models*

398 The first two stages of our accretion law are consistent with astrophysical  
399 models that predict (i) a fast initial accretion due to gravitational collapse of  
400 meter to kilometer size boulders (Johansen et al., 2015; Simon et al., 2017)  
401 and (ii) a rather cold and continuous snowball sweeping of dust and pebbles  
402 (Xie et al., 2010). The second stage, corresponding to pebble accretion, can

403 further be interpreted in terms of the evolution of the fraction of pebbles in  
 404 the disk.

405 Visser and Ormel (2016) performed numerical simulations of pebble ac-  
 406 cretion as a function of the sizes of the accreted particles and of the accreting  
 407 planetesimal as well as of the distance from the star. They define and com-  
 408 pute a pebble accretion time scale,

$$t_{growth} = \frac{M}{\dot{M}} = \frac{4\rho_{\bullet}R}{3v_{hw}\rho_p f_{coll}}, \quad (17)$$

409 with  $M$  the mass of the accreting planetesimal,  $\dot{M}$  its time derivative,  $\rho_{\bullet}=1 \text{ g cm}^{-3}$   
 410 the internal density of the pebbles,  $v_{hw}=5780 \text{ cm s}^{-1}$  the magnitude of the  
 411 headwind faced by the planetesimal,  $f_{coll}$  the collisional efficiency, and  $\rho_p$  the  
 412 density of pebbles in the disk (expressed as a relative density compared to  
 413 the gas density  $\rho_g$ ). The value of  $t_{growth}$  depends on the size of the planetes-  
 414 imal, on the solid-to-gas ratio  $\rho_p/\rho_g$ , and on the distance from the star. For  
 415 the sake of the argument, we shall use the results obtained by Visser and  
 416 Ormel (2016) at 3 AU and for a typical planetesimal size of 100 km which is  
 417 relevant for our study and corresponds to a minimal dependence of the result  
 418 on the size of the pebbles. For this choice of parameters, and for a typical  
 419 solid-to-gas  $\rho_p^{ref}/\rho_g = 1/100$ , Visser and Ormel (2016) show in their figure 4  
 420 that the growth timescale  $t_{growth}^{ref}$  ranges between 40 Myr and 100 Myr for  
 421 pebbles radii between 0.01 cm and 30 cm. These time scales are one order  
 422 of magnitude larger than the one estimated by our model. This implies that  
 423 the solid-to-gas ratio during the accretion of iron meteorites was also one  
 424 order of magnitude larger.

425 For a given accretion curve  $R(t)$  obtained by the inversion of the ther-  
 426 mal evolution recorded by the magmatic iron meteorites it is possible to

427 calculate the evolution of the accretion time scale  $t_{growth}(t) = \frac{1}{3}R(t)/\dot{R}(t)$ .  
 428 In the conditions described above, the ratio  $t_{growth}(t)/t_{growth}^{ref}$  is directly the  
 429 ratio  $\rho_p^{ref}/\rho_p(t)$  with  $\rho_p(t)$  the time-varying fraction of pebbles seen by the  
 430 planetesimal during its accretion. As an example, we show in figure 7 the evo-  
 431 lution of  $\rho_p(t)/\rho_g$  for a nucleus of 65 km. As expected, the density of pebbles  
 432 starts with a very high value, consistent with the production of a nucleus by  
 433 gravitational collapse in overdense zones in the disk, and sharply decreases  
 434 around 3 Myr at the end of the accretion. One should note however that this  
 435 marks also the appearance of a new mechanism (sintering and/or erosion)  
 436 that would artificially decrease the effective density of pebbles “seen” by the  
 437 planetesimal.

438 *5.4. Consequences for the differentiation of the parent body of magmatic iron*  
 439 *meteorites*

440 Under canonic nebular conditions, iron can be anticipated to be present  
 441 within these pebbles and dust as metallic Fe (dominant form), FeS and oxi-  
 442 dized Fe in silicates (Ebel, 2006). Upon heating within the planetesimal, it is  
 443 expected that FeS melts first at the corresponding Fe-FeS eutectic  $\approx 1000^\circ\text{C}$   
 444 (Brett and Bell, 1969) (see Supplementary Material, Figure 13). As the tem-  
 445 perature rises, the melt becomes more iron rich. As Kruijer et al. (2014)  
 446 we further assume that the metallic melt remains in contact with the sil-  
 447 icate matrix until the total melting of FeS alloy. Under this assumption,  
 448 the recorded temperature corresponds to the liquidus temperature set by the  
 449 Sulfur content and the Hf-W age to the time at which this liquidus temper-  
 450 ature is reached. This implies that the systematic difference in age between  
 451 the old “non-carbonaceous” (NC) magmatic iron meteorites and the younger

452 “carbonaceous” (CC) magmatic iron meteorites, is not due to a difference  
453 in accretion age, but simply related to the fact that NC are richer in S, and  
454 thus reached their FeS liquidus temperature earlier than CC.

455 It is worth noting that metallic melt separation that occurs at liquidus  
456 temperature does not necessarily correspond to total differentiation, thus  
457 the Hf-W age does not correspond to the age of core formation, but rather  
458 to the formation of metal pockets large enough to prevent metal-silicate W  
459 re-equilibration. Eutectic melting of Fe-FeS can take place much below the  
460 temperature of melting of the silicate framework which may indeed hamper  
461 the percolation of the Fe-FeS liquids to the core. The problem of the differ-  
462 entiation of an accreting planetesimal has been previously addressed using a  
463 purely conductive model, pure Fe metal only and no surface tension (Sramek  
464 et al., 2012) for a 500 km planetesimal that accreted within 3 Myr. Their  
465 results can be used to discuss the process of compaction and core formation  
466 in our scenario. At 3 My, about half of the metal is molten and has segre-  
467 gated to form a central core and a non negligible part of the molten metal  
468 is furthermore trapped in the solid silicate matrix as lenses at intermediate  
469 depths. It is very likely that metal extraction will be even less efficient in  
470 our model for two reasons. First, all things being equal, the average inter-  
471 nal temperature in a convective planetesimal (our case) is smaller than in a  
472 conductive one (the case studied in Sramek et al. (2012)). Hence the rate of  
473 production of molten metal, and the subordinated rate of metal extraction,  
474 will be smaller in the convective than in the conductive regime. As a con-  
475 sequence differentiation will take a longer time in a convective planetesimal  
476 and will have reached a less advanced stage when cooling and solidification

477 will occur. Second, it has been theoretically established that high surface  
478 tension (such as the one between solid silicate and Fe-FeS metal) enhances  
479 local melt concentration rather than global melt extraction (Ricard et al.,  
480 2001). Experiments have further shown that a threshold fraction of about  
481 15 vol% of Fe-S melt was required to overcome surface tension effects and to  
482 extract the melt from the solid silicate matrix (Bagdassarov et al., 2009). We  
483 can thus conclude that in our model complete melting of the Fe-FeS mixture  
484 is a necessary condition for an efficient compaction leading to the formation  
485 of a core. However, melting of more than 50% of the silicate matrix will  
486 be further necessary to yield complete metal extraction and full differentia-  
487 tion (Sramek et al., 2012), as in that case percolation is not limited by the  
488 rheology of the matrix anymore.

489 Based on the previous arguments, we conclude that the parent bodies of  
490 magmatic iron meteorites might be only partially differentiated, some iron  
491 meteorites being possibly fragments of local ponds of molten metal rather  
492 than pieces of the central core (figure 4). This conclusion is in fact not spe-  
493 cific to the present accretion model. In the models considered up to now for  
494 the formation of the parent bodies of iron meteorites, i. e., instantaneous ac-  
495 cretion at given times (Kruijer et al., 2014), the thermal evolution calculated  
496 taking into account convection predicts much lower average internal temper-  
497 atures than previously anticipated in purely conductive models (Figure 2).  
498 In a scenario of instantaneous accretion, total melting and full differentiation  
499 occurred only for the “non carbonaceous” magmatic iron meteorites.

500 The present accretion model, while developed to reproduce the thermal  
501 histories of the parent bodies of magmatic iron meteorites, seems to explain

502 also correctly two major characteristics of the parent bodies of CV carbona-  
503 ceous chondrites, namely (i) the age of the end of their accretion and (ii)  
504 the coexistence of an external undifferentiated shell with a central convective  
505 metallic core potentially powering a dynamo (Gattacceca et al., 2016). In  
506 our scenario, convection develops in the planetesimal underneath a stable  
507 conductive viscous lid of a few kilometer thickness (Supplementary Material  
508 Figure 14). The interior of this viscous lid is by definition much colder than  
509 the interior of the body hence cannot reach the solidus and remains undif-  
510 ferentiated. The distribution of  $^{26}\text{Al}$  ages in chondrules from CV chondrites  
511 implies that accretion of their parent body was still ongoing  $\approx 4$  Myr after  
512 CAIs (Villeneuve et al., 2009). In our model this would correspond to the  
513 very last stage of limited accretion occurring between  $\approx 3$  and 4 Myr, once  
514 sintering has become the dominant feature. At 4 Myr, the  $300^\circ\text{C}$  isotherm in  
515 the viscous lid is located  $\approx 2\text{-}3$  km below the surface, allowing the preserva-  
516 tion of primitive accreted materials including chondrules and of undisturbed  
517  $^{26}\text{Al}$  isochrons in these chondrules (Supplementary Material Figure 14). Such  
518 a planetesimal would have developed a metallic core which could remain par-  
519 tially melted long enough for a dynamo to develop in agreement with recent  
520 paleomagnetic observations in chondrules from CV chondrites (Gattacceca  
521 et al., 2016). It is worthwhile noting that the presence of a stagnant lid and  
522 of internal heating reduce the amount of heat that can be extracted from  
523 the core and transported by convection to the surface. In some cases, if the  
524 internal heating is too high, the heat flux at the boundary between the core  
525 and the mantle may even be negative, i.e. the core is heating up, which  
526 would then help to keep it molten for longer periods of time.

527 **6. Conclusion**

528 We have developed a model for the transient thermal evolution of a plan-  
529 etesimal in the course of accretion. Compared to previous approaches, the  
530 model takes into account both a conductive regime (at the beginning of ac-  
531 cretion when temperature increase and radius are small) and a convective  
532 regime. Although convection is not necessarily required by our model, for  
533 nominal values of the parameters that enter the experimentally derived scal-  
534 ing laws, convection would start around 1 Myr during the accretion.

535 We show that the thermal evolution recorded by all the magmatic iron  
536 meteorites can be described by a unique exponential law that we latter em-  
537 ployed to obtain accretion curves using the conservation of energy in the  
538 parent bodies of the magmatic iron meteorites. Once made dimensionless,  
539 all the accretion curves define a universal accretion law that introduces three  
540 stages: (i) instantaneous nucleus formation at  $t=0$  by gravitational collapse,  
541 (ii) continuous pebble accretion at a rate decreasing with time and ending  
542 at  $\approx 3$  Myr, (iii) negligible accretion accompanied by a few percent sintering  
543 by compaction.

544 A main difference of our model compared to previous predictions of mod-  
545 els that considered instantaneous accretion and a purely conductive thermal  
546 regime is a colder thermal evolution controlled by the continuous accretion  
547 of cold “pebbles”, and that may yield partial differentiation only. Some of  
548 the magmatic iron meteorites may thus be local metal ponds rather than the  
549 remnant of the metallic core of their parent body.

550 Furthermore, regardless the cooling mode (conduction or convection) in  
551 the parent body, there will always exist a cold viscous stagnant lid of a few

552 kilometers that should have remained completely undifferentiated.

553 On another hand the presence of a stagnant lid may also delay the cooling  
554 of the planetesimal even if cooling proceeds by convection. If such a plan-  
555 etesimal is differentiated, then the metallic core can develop a dynamo for a  
556 non-negligible amount of time.

557 Partial melting of the silicate phase will produce a certain degree of sil-  
558 icate differentiation in addition to the formation of an iron core. Hence  
559 multi-phase flow modeling will be required to further describe the thermal  
560 evolution of the planetesimal during that stage. Such a complex modeling  
561 remains however beyond the scope of this study.

562 More generally, our formalism which combines convective thermal trans-  
563 fer and the evolution of the size of the body during its formation, could be  
564 used to compute the thermal evolution produced by a given accretion law,  
565 hence to provide additional constraints for theoretical models of planetesi-  
566 mals formation and evolution.

## 567 **Acknowledgment**

568 We would like to thank the reviewers and the editor William B. McK-  
569 innon for their fruitful comments that improved the manuscript. This work  
570 was funded by the ANR-11-IS04-0004 project and supported by the Tel-  
571 lus/PNP program of INSU-CNRS. Many thanks to Medi@Terre for improv-  
572 ing Figure 4. This project contributes to the IdEx project Université de Paris  
573 ANR-18-IDEX-0001.

574 **References**

- 575 Bagdassarov, N., Golabek, G. J., Solferino, G., Schmidt, M. W., 2009. Con-  
576 straints on the FeS melt connectivity in mantle silicates from electrical  
577 impedance measurements. *Phys. Earth Planet. Int.* 177, 139–146.
- 578 Birnstiel, T., Fang, M., Johansen, A., 2016. Dust evolution and the formation  
579 of planetesimals. *Space Sci. Rev.* 205, 41–75.
- 580 Brett, R., Bell, P. M., 1969. Melting relations in the Fe-rich portion of the  
581 system Fe-FeS at 30 kb pressure. *Earth Planet. Sci. Lett.* 6, 479–482.
- 582 Budde, G., Burkhardt, C., Brennecka, G. A., Fischer-Gödde, M., Kruijer,  
583 T. S., Kleine, T., 2016. Molybdenum isotopic evidence for the origin  
584 of chondrules and a distinct genetic heritage of carbonaceous and non-  
585 carbonaceous meteorites. *Earth and Planetary Science Letters* 454, 293–  
586 303.
- 587 Carslaw, H. S., Jaeger, J. C., 1959. *Conduction of heat in solids.* Oxford  
588 University Press, New York.
- 589 Choblet, G., Sotin, C., 2000. 3D thermal convection with variable viscosity:  
590 can transient cooling be described by a quasi-static scaling law? *Phys.*  
591 *Earth Planet. Int.* 119, 321–336.
- 592 Cuzzi, J. N., Hogan, R. C., Shariff, K., 2008. Toward planetesimals: dense  
593 chondrules clumps in the protoplanetary nebula. *Astrophys. J.* 687, 1432–  
594 1447.

- 595 Davaille, A., Jaupart, C., 1993. Transient high-Rayleigh-number thermal con-  
596 vection with large viscosity variations. *J. Fluid Mech.* 253, 141–166.
- 597 Delbo', M., Walsh, K., Avdellidou, C., Morbidelli, A., 2017. A major asym-  
598 metric dust trap in a transition disk. *Science* 357, 1026–1029.
- 599 Deschamps, F., Yao, C., Tackley, P. J., Sanchez-Valle, C., 2012. High  
600 Rayleigh number thermal convection in volumetrically heated spherical  
601 shells. *J. Geophys. Res.* 117, E09006.
- 602 Ebel, D. S., 2006. Condensation of rocky materials in astrophysical environ-  
603 nments. In: Lauretta, D. S., McSween, H. Y. J. (Eds.), *Meteorites and the*  
604 *early Solar System II*. University of Arizona Press, Tucson, pp. 253–277.
- 605 Gattacceca, J., Weiss, B. P., Gounelle, M., 2016. New constraints on the  
606 magnetic history of the cv parent body and the solar nebula from the  
607 Kaba meteorite. *Earth Planet. Sci. Lett.* 455, 166–175.
- 608 Ghosh, A., Weidenschilling, S. J., McSween Jr, H. Y., 2003. Importance of  
609 the accretion process in asteroid thermal evolution: 6 Hebe as an example.  
610 *Meteorit. Planet. Sci.* 38, 711–724.
- 611 Goldstein, J. I., Scott, E. R. D., Chabot, N. L., 2009. Iron meteorites:  
612 Crystallization, thermal history, parent bodies, and origin. *Chem Erde*  
613 - *Geochem.* 69, 293–325.
- 614 Haack, H., Rasmussen, K. L., Warren, P. H., 1990. Effects of regolith megare-  
615 golith insulation on the cooling histories of differentiated asteroids. *J. Geo-*  
616 *phys. Res.* 95, 5111–5124.

- 617 Hevey, P. J., Sanders, I. S., 2006. A model for planetesimal meltdown by  
618  $^{26}\text{Al}$  and its implications for meteorite parent bodies. *Meteorit. Planet.*  
619 *Sci.* 41, 95–106.
- 620 Hustoft, J., Scott, T., Kohlstedt, D. L., 2007. Effect of metallic melt on the  
621 viscosity of peridotite. *Earth Planet Sci. Lett.* 260, 355–360.
- 622 Johansen, A., Lambrechts, M., 2017. Forming planets via pebble accretion.  
623 *Annu. Rev. Earth Planet. Sci.* 12451, 359–387.
- 624 Johansen, A., Mac Low, M. M., Lacerda, P., Bizzarro, M., 2015. Growth  
625 of asteroids, planetary embryos, and Kuiper belt objects by chondrule  
626 accretion. *Sci. Adv.* 1:e1500109.
- 627 Kleine, T., Münker, C., Mezger, K., Palme, H., 2002. Rapid accretion and  
628 early core formation on asteroids and the terrestrial planets from Hf-W  
629 chronometry. *Nature* 418, 952–955.
- 630 Kruijer, T. S., Burkhardt, C., Budde, G., Kleine, T., 2017. Age of Jupiter  
631 inferred from the distinct genetics and formation times of meteorites. *Proc.*  
632 *Natl. Acad. Sci. USA* 114, 6712–6716.
- 633 Kruijer, T. S., Touboul, M., Fischer-Gödde, M., Bermingham, K. R., Walker,  
634 R. J., Kleine, T., 2014. Protracted core formation and rapid accretion of  
635 protoplanets. *Science* 344, 1150–1154.
- 636 Lee, D. C., Halliday, A. N., 1997. Core formation on Mars and differentiated  
637 asteroids. *Nature* 388, 854–857.

638 Lichtenberg, T., Golabek, G. J., Gerya, T. V., Meyer, M. R., 2016. The effects  
639 of short-lived radionuclides and porosity on the early thermo-mechanical  
640 evolution of planetesimals. *Icarus* 274, 350–365.

641 Limare, A., Kenda, B., Kaminski, E., Surducan, E., Surducan, V., Neamtu,  
642 C., 2020. Transient lab-scale experiments of internally heated convection.  
643 submitted to *MethodsX*.

644 Limare, A., Vilella, K., Di Giuseppe, E., Farnetani, C. G., Kaminski, E.,  
645 Surducan, E., Surducan, V., Neamtu, C., Fourel, L., Jaupart, C., 2015.  
646 Microwave-heating laboratory experiments for planetary mantle convec-  
647 tion. *J. Fluid Mech.* 777, 50–67.

648 McSween, H. Y. J., 1999. *Meteorites and their parent planets*. Cambridge  
649 University Press, Cambridge.

650 Merk, R., Breuer, D., Spohn, T., 2002. Numerical modeling of  $^{26}\text{Al}$ -induced  
651 melting of asteroids considering accretion. *Icarus* 159, 183–191.

652 Morbidelli, A., Raymond, S. N., 2016. Challenges in planet formation. *J.*  
653 *Geophys. Res. Planets* 121, 1962–1980.

654 Ormel, C. W., Klahr, H. H., 2010. The effect of gas drag on the growth of  
655 protoplanets. analytical expressions for the accretion of small bodies in  
656 laminar disks. *Astron. Astrophys.* 520, A43.

657 Parmentier, E. M., Sotin, C., 2000. Three-dimensional numerical experiments  
658 on thermal convection in a very viscous fluid: Implications for the dynamics  
659 of a thermal boundary layer at high Rayleigh number. *Phys. Fluids* 12 (3),  
660 609–617.

- 661 Qin, L., Dauphas, N., Wadhwa, M., Masarik, J., Janney, P. E., 2008. Rapid  
662 accretion and differentiation of iron meteorite parent bodies inferred from  
663  $^{182}\text{Hf}$ - $^{182}\text{W}$  chronometry and thermal modeling. *Earth Planet. Sci. Lett.*  
664 273, 94–104.
- 665 Ricard, Y., Bercovici, D., Schubert, G., 2001. A two-phase model for com-  
666 paction and damage 2. Applications to compaction, deformation, and the  
667 role of interfacial surface tension. *J. Geophys. Res.* 106, 8907–8924.
- 668 Schubert, G., Turcotte, D. L., Olson, P., 2001. *Mantle convection in the*  
669 *Earth and planets*. Cambridge University Press, Cambridge.
- 670 Scott, T., Kohlstedt, D. L., 2006. The effect of large melt fraction on the  
671 deformation behavior of peridotite. *Earth Planet Sci. Lett.* 216, 177–187.
- 672 Simon, J. P., Armitage, P. J., Youdin, A. N., Rixin, L., 2017. Evidence for  
673 universality in the initial planetesimal mass function. *Astrophys. J. Lett.*  
674 847, L12.
- 675 Sramek, O., Milelli, L., Richard, Y., Labrosse, L., 2012. Thermal evolution  
676 and differentiation of planetesimals and planetary embryos. *Icarus* 217,  
677 339–354.
- 678 Suzuki, A., Ohtani, E., Kato, T., 1998. Density and thermal expansion of a  
679 peridotite melt at high pressure. *Phys. Earth Planet. Int.* 107, 53–61.
- 680 van der Marel, N., et al., 2013. A major asymmetric dust trap in a transition  
681 disk. *Science* 340, 1199–1202.

- 682 Vilella, K., Kaminski, E., 2017. Fully determined scaling laws for volumet-  
683 rically heated convective systems, a tool for assessing habitability of exo-  
684 planets. *Phys. Earth Planet. Int.* 266, 18–28.
- 685 Vilella, K., Limare, A., Jaupart, C., Farnetani, C., Fourel, L., Kaminski, E.,  
686 2018. Fundamentals of laminar free convection in internally heated fluids  
687 at values of the RayleighRoberts number up to  $10^9$ . *J. Fluid Mech.* 846,  
688 966–998.
- 689 Villeneuve, J., Chaussidon, M., Libourel, G., 2009. Homogeneous distribu-  
690 tion of Al-26 in the solar system from the Mg isotopic composition of  
691 chondrules. *Science* 325, 985–988.
- 692 Visser, R. G., Ormel, C. W., 2016. On the growth of pebble-accreting plan-  
693 etesimals. *Astron. Astrophys.* 586, A66, 1–11.
- 694 Weidenschilling, S. J., 1977. Aerodynamics of solid bodies in the solar nebula.  
695 *Mon. Not. R. Astron. Soc.* 180, 57–70.
- 696 Xie, J. W., Payne, M. J., Thébault, P., Zhou, J. L., Ge, J., 2010. From dust  
697 to planetesimals: the snowball phase? *Astrophys. J.* 724, 1153–1164.
- 698 Yang, J., Goldstein, J. I., 2006. Metallographic cooling rates of the IIIAB  
699 iron meteorites. *Geochim. Cosmochim. Acta* 70, 3197–3215.
- 700 Yang, J., Goldstein, J. I., Michael, J. R., Kotula, P. G., Scott, E. R. D.,  
701 2010. Thermal history and origin of the IVB iron meteorites and their  
702 parent body. *Geochim. Cosmochi. Acta* 74, 4493–4506.

703 Yang, J., Goldstein, J. I., Scott, E. R. D., 2008. Metallographic cooling rates  
704 and origin of IVA iron meteorites. *Geochim. Cosmochim. Acta* 72, 3043–  
705 3061.

Table 1: Definition and values of the model parameters or formulae used to compute them.

References: <sup>+</sup> Sramek et al. (2012), <sup>o</sup> Suzuki et al. (1998), \* www.nucleide.org

Quantity	Symbol	Units	Value / Formula
Metal mass <sup>+</sup> , volume fraction	$x^{\text{met}}, \phi^{\text{met}}$	-	$x^{\text{met}}=0.18$
Silicate mass <sup>+</sup> , volume fraction	$x^{\text{sil}}, \phi^{\text{sil}}$	-	$x^{\text{sil}}=0.82$
Average porosity	$\phi$	-	0.1
Density of metal <sup>+</sup>	$\rho^{\text{met}}$	kg m <sup>-3</sup>	7800
Density of silicate <sup>+</sup>	$\rho^{\text{sil}}$	kg m <sup>-3</sup>	3200
Average density	$\rho$	kg m <sup>-3</sup>	$1/\rho = x^{\text{met}}/\rho^{\text{met}} + x^{\text{sil}}/\rho^{\text{sil}}$
Specific heat of metal <sup>+</sup>	$C_p^{\text{met}}$	J K <sup>-1</sup> kg <sup>-1</sup>	450
Specific heat of silicate <sup>+</sup>	$C_p^{\text{sil}}$	J K <sup>-1</sup> kg <sup>-1</sup>	1200
Average specific heat	$C_p$	J K <sup>-1</sup> kg <sup>-1</sup>	$C_p = x^{\text{met}}C_p^{\text{met}} + x^{\text{sil}}C_p^{\text{sil}}$
Latent heat of metal <sup>+</sup>	$L^{\text{met}}$	kJ kg <sup>-1</sup>	250
Latent heat of silicate <sup>+</sup>	$C_p^{\text{sil}}$	kJ kg <sup>-1</sup>	500
Activation energy metal	$E_{act}^{\text{met}}$	kJ mol <sup>-1</sup>	13
Activation energy silicate	$E_{act}^{\text{sil}}$	kJ mol <sup>-1</sup>	250
Average activation energy	$E_{act}$	kJ mol <sup>-1</sup>	$E_{act} = \phi^{\text{met}}E_{act}^{\text{met}} + \phi^{\text{sil}}E_{act}^{\text{sil}}$
Thermal conductivity of metal <sup>+</sup>	$k^{\text{met}}$	J s <sup>-1</sup> m <sup>-1</sup> K <sup>-1</sup>	50
Thermal conductivity of silicate <sup>+</sup>	$k^{\text{sil}}$	J s <sup>-1</sup> m <sup>-1</sup> K <sup>-1</sup>	3
Average thermal conductivity	$k$	J s <sup>-1</sup> m <sup>-1</sup> K <sup>-1</sup>	$k = \phi^{\text{met}}k^{\text{met}} + \phi^{\text{sil}}k^{\text{sil}}$
Thermal diffusivity	$\kappa$	m <sup>2</sup> s <sup>-1</sup>	$\kappa = k/(\rho C_p)$
Dynamic viscosity	$\mu$	Pa s	
Kinematic viscosity	$\nu$	m <sup>2</sup> s <sup>-1</sup>	$\nu = \mu/\rho$
Coefficient of thermal expansion <sup>o</sup>	$\alpha$	K <sup>-1</sup>	$3 \cdot 10^{-5}$
Acceleration of gravity	$g$	m s <sup>-2</sup>	$g = 4/3\pi RG\rho$
Universal gravity constant	$G$	m <sup>3</sup> kg <sup>-1</sup> s <sup>-2</sup>	$6.674 \cdot 10^{-11}$
Initial radiogenic heat production	$H_0$	J s <sup>-1</sup> kg <sup>-1</sup>	$1.5 \cdot 10^{-7}$
<sup>26</sup> Al decay constant*	$\lambda$	s <sup>-1</sup>	$3 \cdot 10^{-14}$
Radiogenic heat production	$H$	J s <sup>-1</sup> kg <sup>-1</sup>	$H(t) = H_0 \exp(-\lambda t)$
Time since CAI formation	$t$	s (Myr)	
Parent body average internal temperature	$T$	°C	
Parent body surface temperature	$T_S$	°C	0
Parent body surface heat flux	$Q_S$	J s <sup>-1</sup> m <sup>-2</sup>	
Parent body radius	$R$	m	
Initial parent body radius	$R_0$	m	$R_0 = R(t=0)$
Rayleigh-Roberts number	$Ra_H$	-	$Ra_H = \frac{\rho g \alpha H R^5}{k \kappa \nu}$

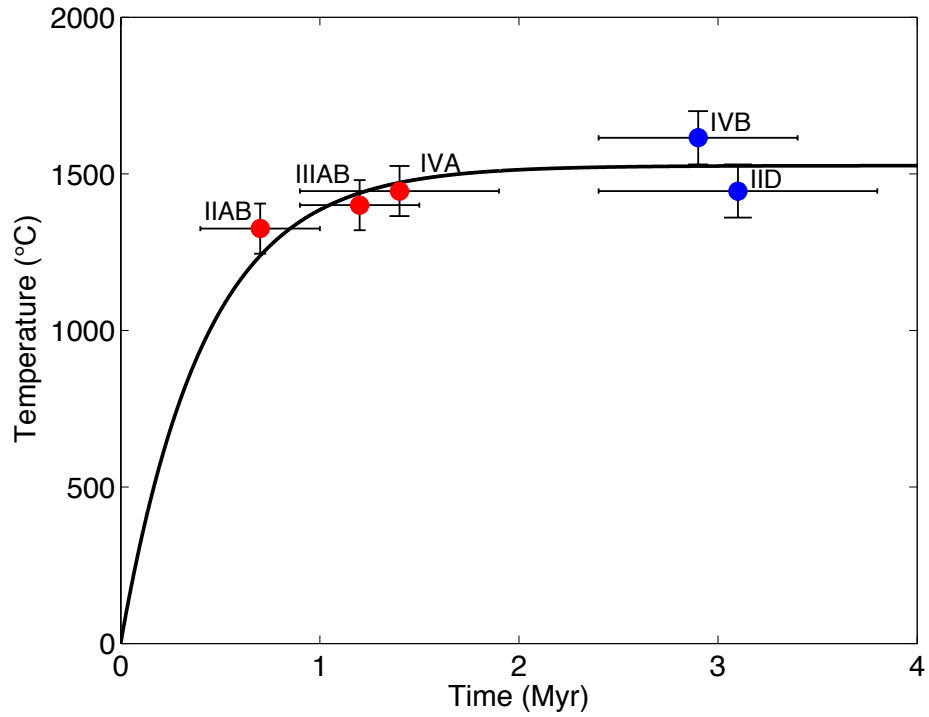


Figure 1: Thermal evolution of the parent body of the iron magmatic meteorites,  $T(t) = T_{\infty}[1 - \exp(-t/\tau)]$ , with  $T_{\infty}=1524^{\circ}\text{C}$  and  $\tau=0.424$  Myr. The red circles give the position of the “non-carbonaceous” magmatic iron meteorites and the blue circles of the “carbonaceous” magmatic iron meteorites (Kruijer et al., 2014; Budde et al., 2016).

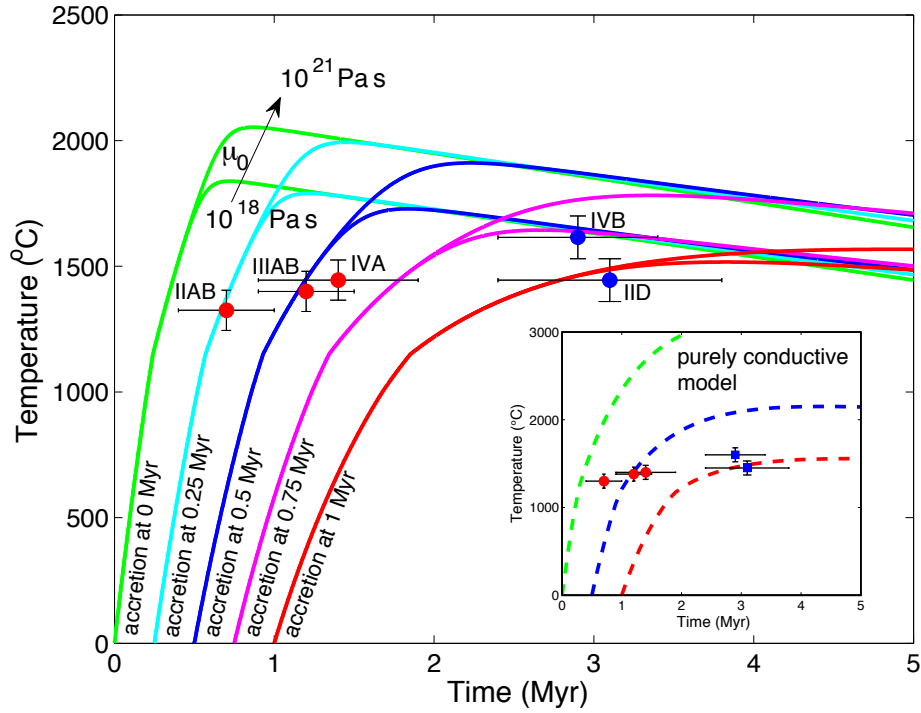


Figure 2: Evolution of the average internal temperature of a 300 km radius planetesimal as a function of its time of instantaneous accretion, and for two values of the reference viscosity  $\mu_0$ . The red circles give the position of the “non-carbonaceous” magmatic iron meteorites and the blue circles of the “carbonaceous” magmatic iron meteorites. Compared to a purely conductive model (dashed lines in the inset, with colors corresponding to the same age of formation as in the main figure) the average internal temperature is much lower when convection is taken into account. This is due to more effective heat transfer to the surface in the convective regime than in the conductive one.

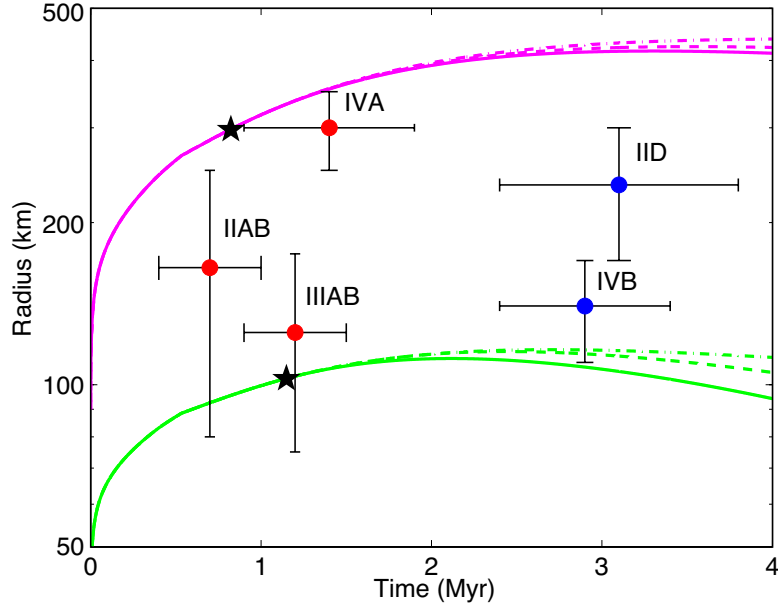


Figure 3: Model results for continuous pebble accretion. The red circles give the position of the “non-carbonaceous” magmatic iron meteorites and the blue circles of the “carbonaceous” magmatic iron meteorites (Kruijer et al., 2014; Budde et al., 2016; Yang et al., 2008, 2010); time is given by the Hf-W age. The accretion curves are a function of the initial (nucleus) radius of the parent body. The green and magenta correspond to a nucleus size of 35 km and 90 km, respectively. The dash-dotted lines give the purely conductive solution, while the dashed and solid lines give the complete solutions with a convective stage for a reference viscosity  $\mu_0$  of  $10^{19}$  and  $10^{18}$  Pa s, respectively. The stars indicate the onset on convection for a reference viscosity of  $10^{18}$  Pa s. For nucleus radii smaller than  $\approx 35$  km the thermal evolution implies a too large sintering of the parent body and is not consistent with our model framework.

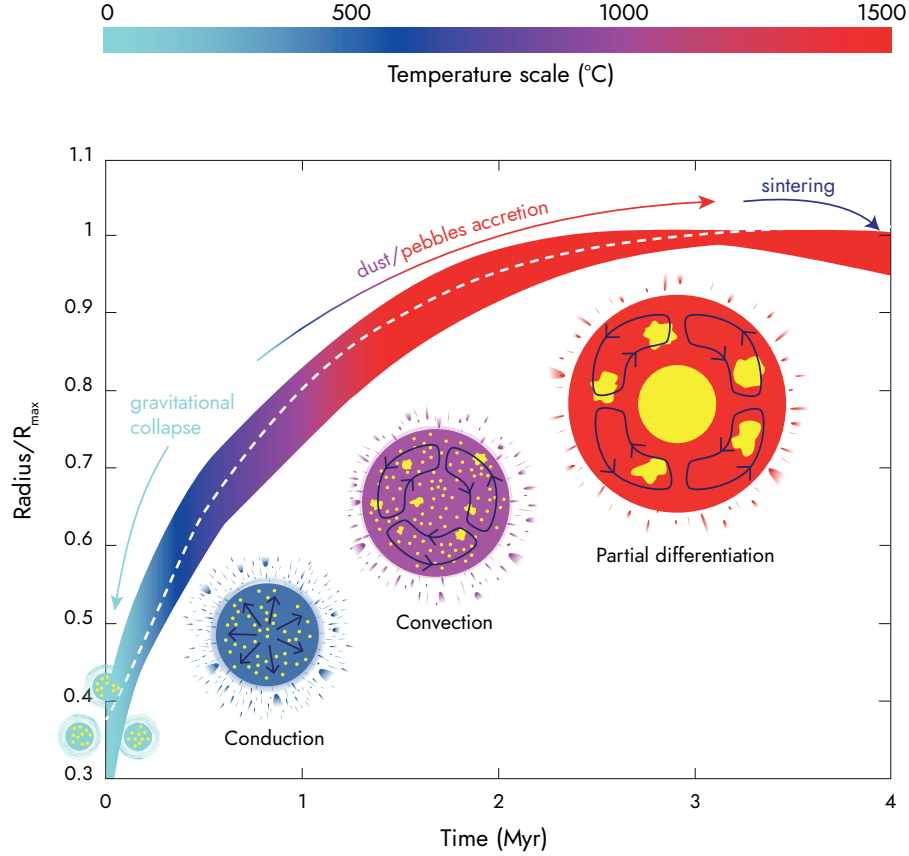


Figure 4: Universal dimensionless accretion curve predicted by the model (colored thick curve) compared to the parameterized accretion law (dashed white line) of the form  $(R(t)/R_{\infty})^3 = 1 - (1 - [R_0/R_{\infty}]^3) \exp(-[t/t_a]^b)$ , where  $t_a = 1.39 \pm 0.15$  Myr is the timescale of accretion,  $b = 1.45 \pm 0.15$  is a shape parameter, and  $R_0$  and  $R_{\infty}$  the initial and final radius, respectively, with  $R_0/R_{\infty} = 0.37 \pm 0.04$ . The color of the curves gives the average internal temperature reached in the parent body at a given time (or equivalently for a given radius). The thickness of the colored curve corresponds to the second order variation of the accretion history for different sizes of the initial nucleus.

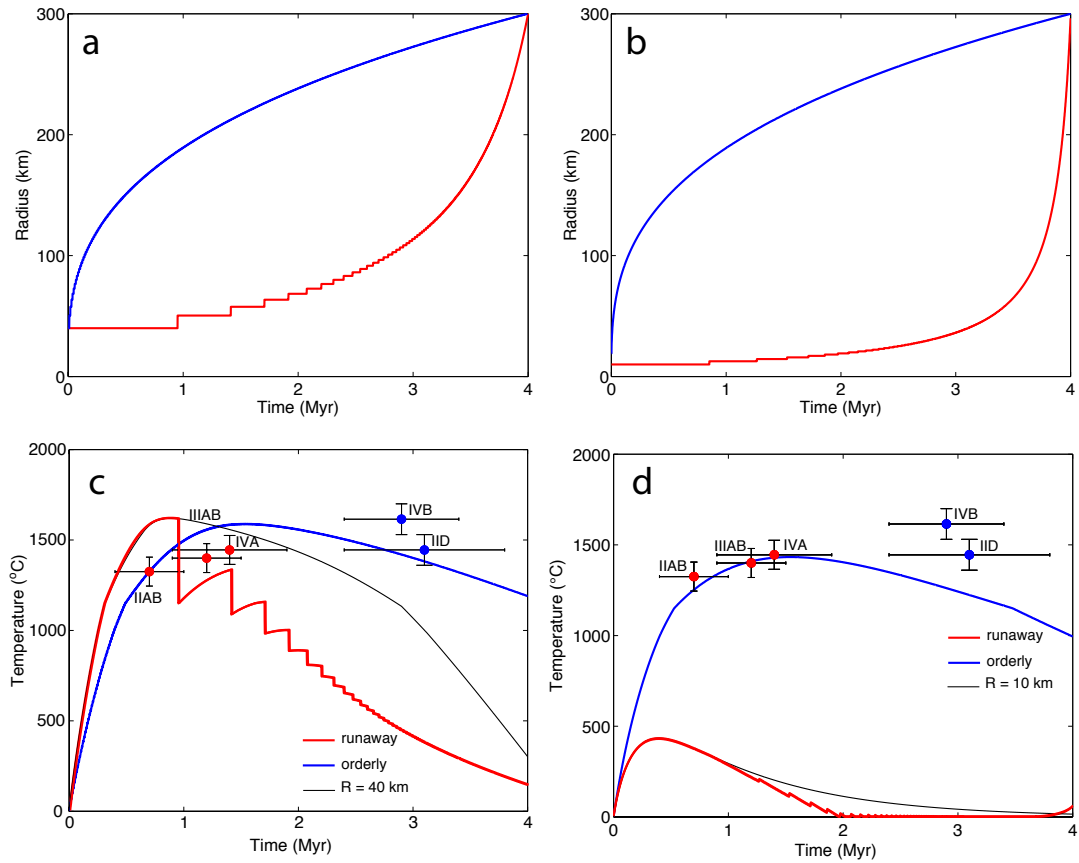


Figure 5: Alternative accretion scenarios. Upper panel: evolution of the radius of the planetesimal as a function of time for the two types of accretion considered: orderly (blue curve) and runaway (red). Lower panel: corresponding thermal evolution. The thin black line gives the evolution of the temperature of the impactor in the case of orderly accretion. (a,c) Results for 40 km impactors: the initial thermal evolution is too fast and leads to massive melting not consistent with the geochemical constraints. (b,d) Results for 10 km impactors: orderly accretion generates a scenario consistent with the parent bodies of NC iron magnetic meteorites only.

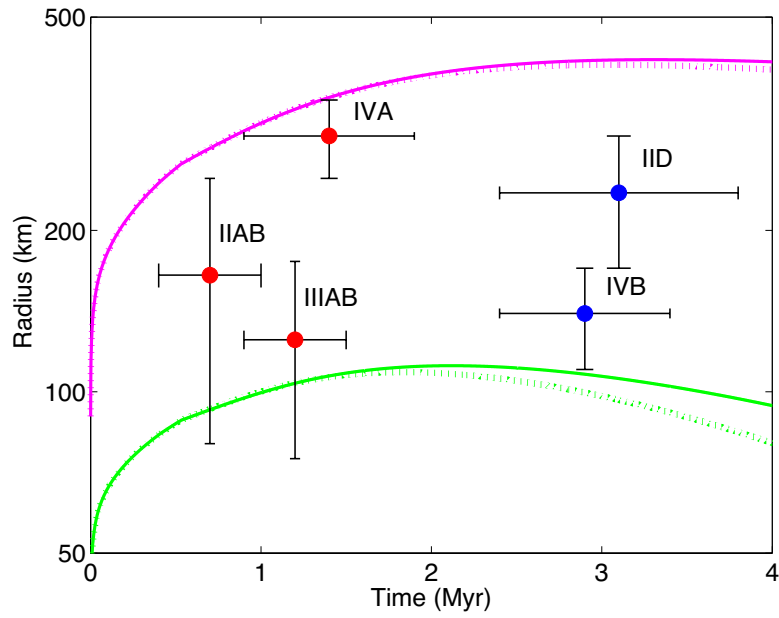


Figure 6: Evolution of the accretion curves when differentiation is taken into account (dotted lines) compared to the reference evolution without differentiation (solid lines). In these calculation differentiation occurs instantaneously when the solidus of the silicate is reached ( $T=1150^{\circ}\text{C}$ ). Differentiation produces a larger sintering at the end of the accretion in small bodies.

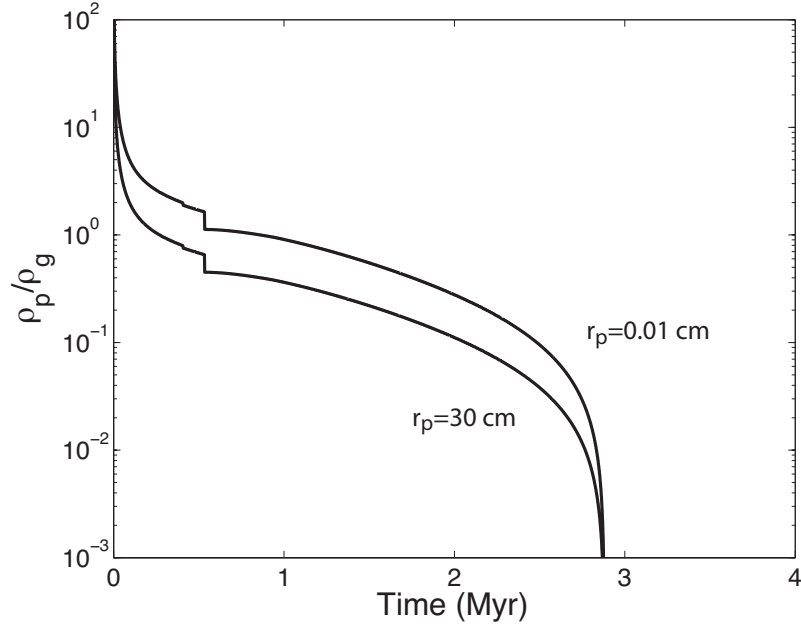


Figure 7: Evolution of the density of pebbles in the disk at 3 AU for a nucleus of 65 km that grows by pebble accretion following the accretion curve based on the inversion of the thermal record of magmatic iron meteorites for a reference viscosity  $\mu_0=10^{19}$  Pa s. Two values of the pebbles radius  $r_p$  are considered, 0.01 cm and 30 cm. The pebbles density is very high at the beginning of the accretion – in agreement with the hypothesis of boulders accretion in dense parts of the disk – and sharply decreases to values  $<10^{-2}$  by the end of accretion at  $\approx 3$  Myr after CAIs. The two steps in the solid line are due to the sharp decrease of viscosity in the planetesimal when iron and then silicate start to melt.

706 **Supplementary Material**

707 Table 2 contains the Hf-W age of formation, Sulfur content and temper-  
708 ature of formation based on the FeS liquidus for the iron meteorites (Krui-  
709 jer et al., 2014). As in Supplementary Material of Kruijer et al. (2014)  
710 ([www.sciencemag.org/content/344/6188/1150/suppl/DC1](http://www.sciencemag.org/content/344/6188/1150/suppl/DC1)) we assume that  
711 the metallic melt remains in contact with the silicate matrix until the total  
712 melting of FeS alloy. Under this assumption, the recorded temperature cor-  
713 responds to the liquidus temperature set by the Sulfur content and the Hf-W  
714 age to the time at which this liquidus temperature is reached.

Table 2: Temperature and age of formation of iron meteorites. Data from Supplementary Material of Kruijer et al. (2014).

Type	Age of formation(Myrs)	Sulfur content (wt%)	$T$ ( $^{\circ}C$ )
IIAB	$0.7 \pm 0.3$	17	$1325 \pm 80$
IIIAB	$1.2 \pm 0.3$	12	$1400 \pm 80$
IVA	$1.4 \pm 0.5$	6	$1445 \pm 85$
IVB	$2.9 \pm 0.5$	0	$1615 \pm 85$
IID	$3.1 \pm 0.7$	7	$1445 \pm 85$

Table 3: Typical size of meteorites estimated from metallographic cooling rates

Type	Radius (km)	Method	Reference
IIAB	$165 \pm 65$	core+mantle	McSween (1999)
IIIAB	$125 \pm 50$	core+mantle	Yang and Goldstein (2006)
IVA	$300 \pm 50$	metallic core ripped of its mantle	Yang et al. (2008)
IVB	$140 \pm 30$	metallic core ripped of its mantle	Yang et al. (2010)
IID	$235 \pm 65$	core+mantle	McSween (1999)

715 Metallographic cooling rates were used to infer the size of the parent bod-  
716 ies of magmatic iron meteorites. These correspond to the latest (conductive)  
717 cooling phase of a metallic pocket (or core) once it has solidified. The size of  
718 the planetesimals have been estimated based on two assumptions (Table 3):  
719 either considering the core with its mantle ripped off, or the cooling of the  
720 core still surrounded by its mantle.

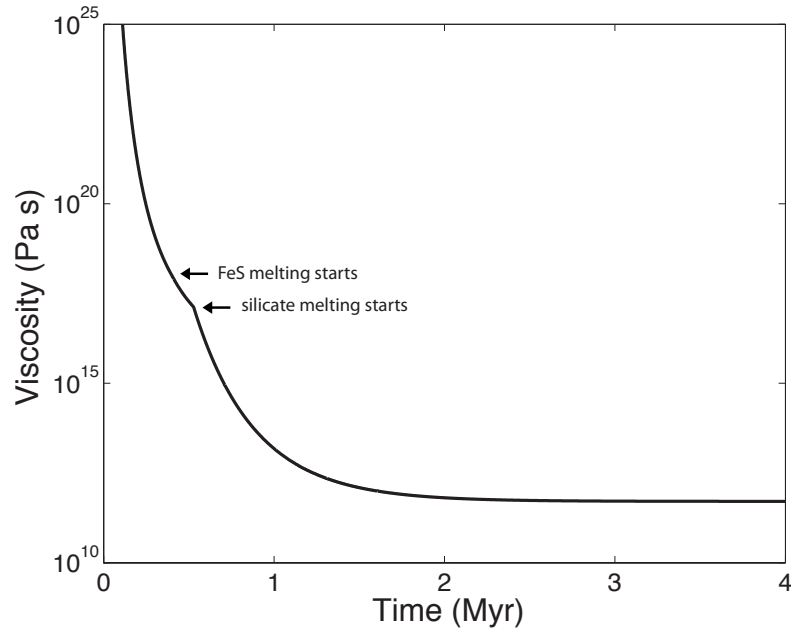


Figure 8: Evolution of the viscosity in the parent body as a function of time for the thermal evolution of figure 1, calculated using equation 11 and for a reference viscosity  $\mu_0 = 10^{18}$  Pa s. The progressive decrease of viscosity is due to (i) the progressive increase of average internal temperature in the body and (ii) the occurrence of Fe-FeS and silicate melting and following increase of melt fraction.

721 Based on the temperature evolution defined in Figure 1, the temperature  
 722 variation of the viscosity translates into the evolution of viscosity with time  
 723 shown in Figure 8.

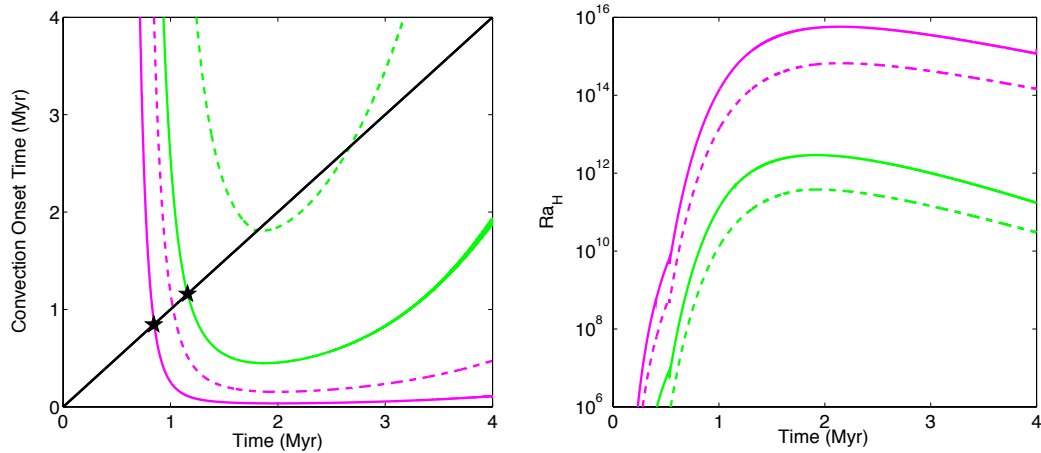


Figure 9: Evolution of the onset time of convection (left) and of the Rayleigh-Roberts number (right) in the parent body as a function of time for the accretion scenarios presented figure 3 and for a reference viscosity  $\mu_0=10^{18}$  Pa s (solid line) and  $10^{19}$  Pa s (dashed line) and two nucleus radii, 35 km (green curves) and 90 km (magenta curves). Stars indicate onset of convection for  $\mu_0=10^{18}$  Pa s.

724 The onset time of convection was calculated using equation16, valid for  
 725 a fluid with strongly temperature depending viscosity. We considered that  
 726 convection starts when the age of the body becomes larger that the onset  
 727 time. The corresponding Rayleigh-Roberts numbers are much larger than  
 728 the critical value for rigid boundary conditions at the surface ( $Ra_{H,cr}=5758$ ).

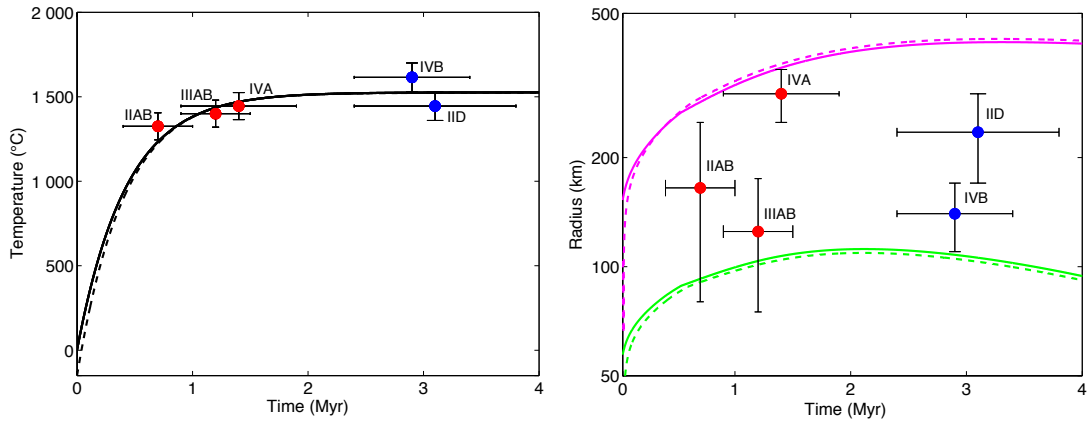


Figure 10: Accretion scenarios obtained from the inversion of the magmatic iron meteorites record considering a surface temperature of  $-150\text{ }^{\circ}\text{C}$  (dashed lines) rather than  $0\text{ }^{\circ}\text{C}$  (solid lines). Thermal evolution of the parent bodies (left panel). The corresponding accretion curves obtained for a model that included convection ( $\mu_0 = 10^{18}\text{ Pa s}$ ) (right panel).

729 We studied the influence of the surface temperature on the thermal evolu-  
 730 tion of the parent bodies of meteorites (Figure 10, left panel). Only negligible  
 731 differences appear in the accretion curves (Figure 10, right panel).

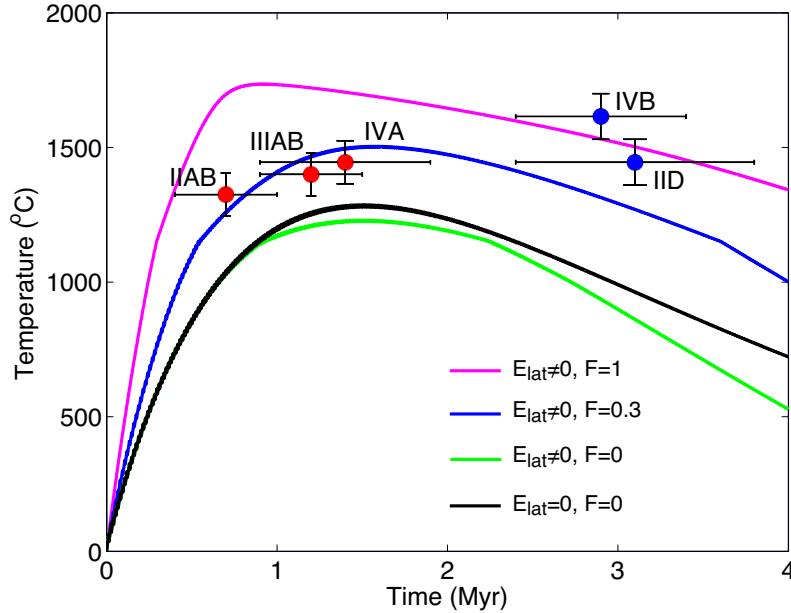


Figure 11: Illustration of the relative contribution of the heat consumed by partial melting,  $E_{lat}$ , and of the heat brought by surface impacts, a fraction  $F$  of this heat being transferred to the target; violet curve:  $F=1$ , blue curve:  $F=0.3$ , green curve:  $F=0$ ). The black curve represents the accretion curve where  $E_{int}=0$ .

732 Two sources of energy have to be added to the conservation energy equa-  
733 tion 2:  $E_{int}=E_{lat}+E_a$ , a term corresponding to the heat absorbed by partial  
734 melting ( $E_{lat}$ ) or brought by surface impacts ( $E_a$ ). We studied the influence  
735 of these energy terms, for an alternative scenario of discontinuous accretion:  
736 orderly accretion of 30km-size impactors that produces a parent body of  
737 300 km in 4 Myr. The results are shown in Figure 11. This scenario pro-  
738 duces a peak temperature more marked than in the scenario of continuous  
739 pebble/dust accretion. A fraction of heat transferred larger than  $\approx 40\%$   
740 is required to fit the NC iron magnetic meteorites constraints, but this implies

741 a too high and too early peak temperature to fit the IVB and IID constraints.  
742 In that scenario the IVB and IID would have been indeed fully molten and  
743 differentiated at  $\approx 2$  Myr and this age would have been recorded by the Hf/W  
744 chronometer. The contribution of the latent heat ( $E_{lat}$ ) is shown by the dif-  
745 ference between the green curve and the black curve ( $E_{lat}=0$  for the black  
746 curve) and is of second order only. Note that the decrease of temperature at  
747 large time is due to efficient heat transfer both in the growing planetesimal  
748 and in the impactors whose temperature becomes smaller and smaller as a  
749 function of time.

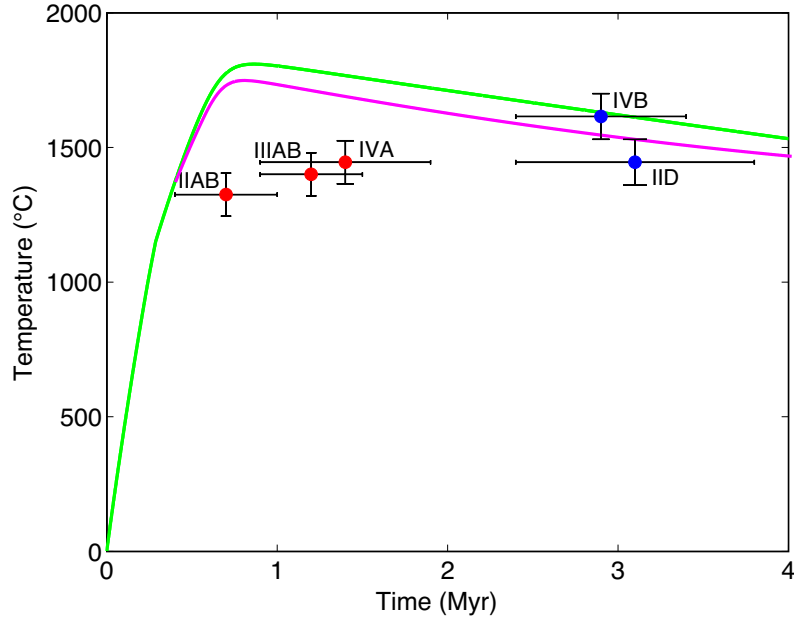


Figure 12: Thermal evolution of a parent body with an initial radius of 300 km fragmented into 27 bodies of 100 km radius at  $t=0.4$  Ma (and using  $\mu_0 = 10^{18}$  Pa s). The magenta line corresponds to the thermal evolution of the 100 km fragments and the green line to that of the residual body.

750 The alternative scenario of fragmentation of a parent body with an initial  
 751 radius of 300 km is shown in Figure 12. Because of the initial large size of  
 752 the body an early total melting occurs which is inconsistent with the ages of  
 753 the magmatic iron meteorites.

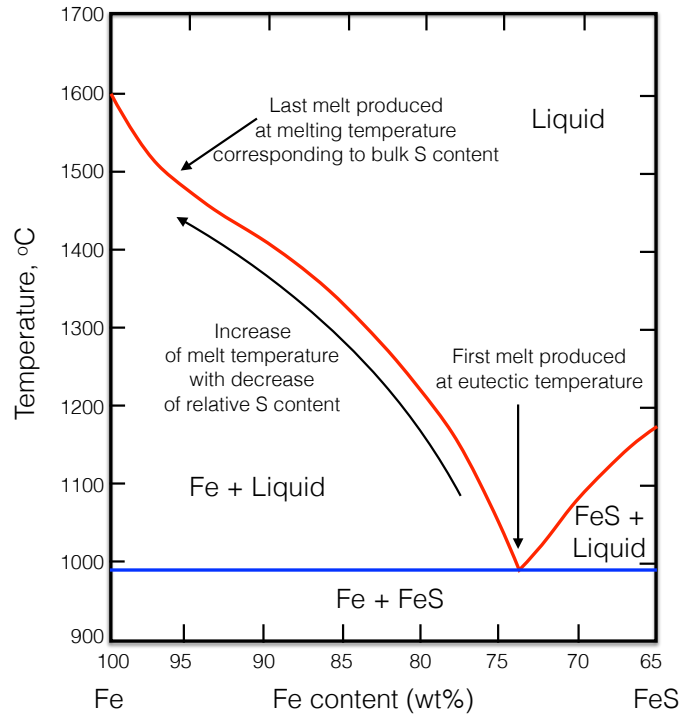


Figure 13: Evolution of the temperature of melting of the metallic phase at 30 kb in the parent body as a function of its sulfur content (Brett and Bell, 1969). The first melt produced is the eutectic  $\approx 74$  wt% of S, whereas the temperature of the last melt produced will be set by the total amount of S in the metallic phase (e.g., 1450 °C for 5 wt% of S).

754 We reproduce here (Figure 13) the phase diagram of the Fe-FeS system  
 755 at a pressure of 30kb obtained by Brett and Bell (1969) and representing the  
 756 data used by Kruijer et al. (2014) for the determination of the temperature  
 757 recorded by the iron meteorites.

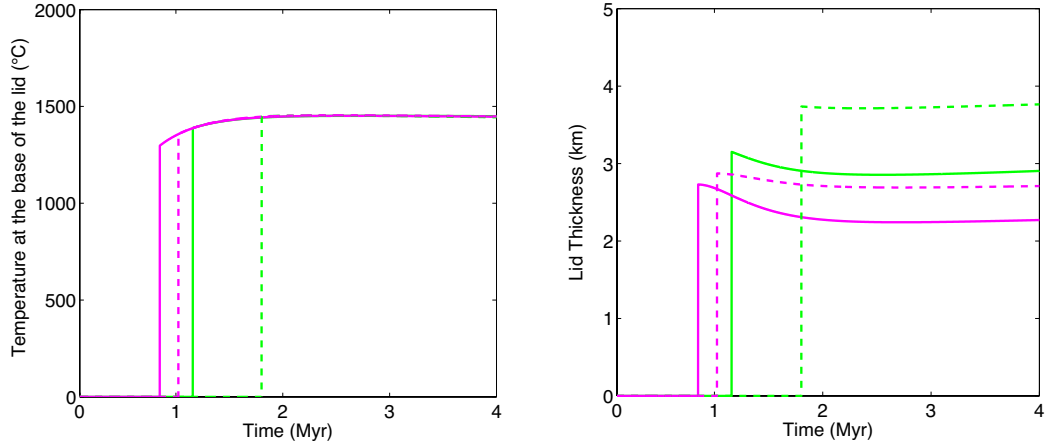


Figure 14: Evolution of the viscous lid thickness and basal temperature once convection has started for the accretion scenario presented Figure 3 and for a reference viscosity  $\mu_0 = 10^{18}$  Pa s (solid line) and  $10^{19}$  Pa s (dashed line) and the two nucleus radius, 35 km (green curves) and 90 km (magenta curves).

758 For a fluid with strongly temperature depending viscosity as the case of  
 759 parent bodies of meteorites, convection takes place under a viscous, stagnant  
 760 lid. The largest part of the viscosity contrast is encompassed by the stagnant  
 761 lid; convection develops preferentially in the least viscous part of the fluid  
 762 layer. The thickness of the lid and temperature at its base are calculated  
 763 according to equation 13 and shown in Figure 14.